

DISCOVERY OF NINE INTERMEDIATE REDSHIFT COMPACT QUIESCENT GALAXIES IN THE SLOAN DIGITAL SKY SURVEY

IVANA DAMJANOV¹, IGOR CHILINGARIAN^{2,3}, HO SEONG HWANG², AND MARGARET J. GELLER²

ABSTRACT

We identify nine galaxies with dynamical masses of $M_{dyn} \gtrsim 10^{10} M_{\odot}$ as photometric point sources, but with redshifts between $z = 0.2$ and $z = 0.6$, in the Sloan Digital Sky Survey (SDSS) spectro-photometric database. All nine galaxies have archival *Hubble Space Telescope* (HST) images. Surface brightness profile fitting confirms that all nine galaxies are extremely compact ($0.4 < R_{e,c} < 6.6$ kpc with the median $R_{e,c} = 0.74$ kpc) for their velocity dispersion ($110 < \sigma < 340$ km s⁻¹; median $\sigma = 178$ km s⁻¹). From the SDSS spectra, three systems are dominated by very young stars; the other six are older than ~ 1 Gyr (two are E+A galaxies). The three young galaxies have disturbed morphologies and the older systems have smooth profiles consistent with a single Sérsic function. All nine lie below the $z \sim 0$ velocity dispersion-half-light radius relation. The most massive system - SDSSJ123657.44+631115.4 - lies right within the locus for massive compact $z > 1$ galaxies and the other eight objects follow the high-redshift dynamical size-mass relation.

Subject headings: galaxies: evolution — galaxies: fundamental parameters — galaxies: stellar content — galaxies: structure

1. INTRODUCTION

The observed strong size evolution of massive quiescent galaxies is a fascinating challenge to our understanding of galaxy formation and evolution (e.g., Khochfar & Silk 2006; Fan et al. 2008; Nipoti et al. 2009; Naab et al. 2009; Hopkins et al. 2010; Oser et al. 2010; Ragone-Figueroa & Granato 2011; Shankar et al. 2012). Daddi et al. (2005) first discovered extremely compact passively evolving systems with half-light radii $R_e < 1$ kpc at redshift $z > 1.4$. Further HST observations show that at a fixed stellar mass, galaxies at zero redshift are generally a factor of 3 – 5 larger than their high redshift counterparts (e.g., Trujillo et al. 2007; Toft et al. 2007; Zirm et al. 2007; Buitrago et al. 2008; Cimatti et al. 2008; van Dokkum et al. 2008; Bezanson et al. 2009; Damjanov et al. 2009, 2011; Carrasco et al. 2010; Strazzullo et al. 2010; Saracco et al. 2011; Cassata et al. 2011; Szomoru et al. 2012; Bruce et al. 2012).

Velocity dispersions measured for small samples of quiescent systems at high redshift confirm that their dynamical masses agree well with the stellar masses derived from SED-fitting (see van de Sande et al. 2013, and the references therein). There are thus two coexisting populations of massive quiescent systems at $z \gtrsim 1$: 1) very dense compact systems and 2) systems with sizes comparable with typical $z \sim 0$ quiescent galaxies (Mancini et al. 2010; Saracco et al. 2011; Cassata et al. 2011; Newman et al. 2012; Onodera et al. 2012).

Compact massive systems seem to disappear by $z \sim 0$, but there are conflicting observations. Trujillo et al. (2009) and Taylor et al. (2010) use the SDSS to suggest that the number density of compact massive sys-

tems at $z < 0.2$ is more than three orders of magnitude below the comoving density at $z \sim 2$. In contrast, from ground-based imaging combined with spectroscopy, Valentinuzzi et al. (2010b) find a significant fraction of compact massive galaxies in the WINGS cluster sample at $z \sim 0.05$; they derive a lower limit on the number density of $n \sim 1.3 \times 10^{-5}$ Mpc⁻³, comparable with the number density of the high-redshift analogs. A similar study of the field population at $0.03 \leq z \leq 0.11$ (Poggianti et al. 2013) suggests that compact dense galaxies exist in this redshift range but their fraction is three times smaller than in the WINGS cluster environment sample.

There are few observational tests of the existence of compact galaxies at redshifts $0.1 \lesssim z \lesssim 1$ (Saglia et al. 2010; Carollo et al. 2013). Valentinuzzi et al. (2010a) identified compact systems with stellar masses $M_{*} > 4 \times 10^{10} M_{\odot}$ among spectroscopically confirmed members of rich galaxy clusters with $0.5 < z < 0.8$. Here we carry out an environment independent search for compact objects in the redshift range $0.2 < z < 0.6$ by combining the photometric and spectroscopic SDSS databases with high-resolution images in the Mikulski Archive for Space Telescopes (MAST). Discovery of dense galaxies in this redshift range is important because larger samples with well-defined selection criteria potentially constrain models of galaxy evolution.

We adopt a $\Omega_{\Lambda} = 0.73$, $\Omega_M = 0.27$, and $H_0 = 70$ km s⁻¹ Mpc⁻¹ cosmology, and quote magnitudes in the AB system.

2. IDENTIFYING COMPACT GALAXY CANDIDATES

We use the SDSS (Release 7; SDSS DR 7) to initiate the search for candidate compact quiescent galaxies in the redshift range $0.2 < z < 0.6$, where the SDSS main sample combined with the BOSS Survey contain spectra for large numbers of objects (Ahn et al. 2013). To identify compact systems we search for objects identified photometrically as stars (in the *PhotoObj* view) but with a redshift in our target range (from the *SpecObj* view).

¹ Harvard-Smithsonian Center for Astrophysics, 60 Garden St., Cambridge, MA 02138

² Smithsonian Astrophysical Observatory, 60 Garden St., Cambridge, MA 02138

³ Sternberg Astronomical Institute, Moscow State University, 13 Universitetsky prospect, 119992 Moscow Russia

Thus we obtain a list of object with sizes less than the SDSS PSF ($\sim 1''.5$). We check that the photometric and spectroscopic objects actually have the same center and that the objects are visually compact in the SDSS images. Additionally we eliminate objects classified spectroscopically as quasars.

To restrict the list to quiescent galaxies, we require that the equivalent width of the $[\text{OII}]\lambda\lambda 3726, 3729$ emission line doublet is $\text{EW}[\text{O II}] < 5 \text{ \AA}$. We check visually that each spectrum has a clear 4000 \AA break along with several absorption features (e.g. Balmer series, Ca H+K and G-band). The final list of SDSS DR7 compact system candidates at $0.2 < z < 0.6$ includes 635 galaxies.

The SDSS photometric dataset provides only an upper limit to the angular size of these systems, corresponding to a physical radius between 2.5 kpc (at $z = 0.2$) and 5 kpc (at $z = 0.6$). To obtain direct size measurement we searched the HST archive. Nine of our 635 candidates have HST images.

Table 2 lists the camera and the filter for each HST observational program together with the corresponding pixel scale. The exquisite HST resolution of $\sim 0''.15$ allows analysis of the structure of these systems on a spatial scale of a few hundred pc ($\lesssim 500 \text{ pc}$ at $z = 0.6$).

3. SPECTROSCOPY AND IMAGING

3.1. The SDSS Spectra

We reanalyze the SDSS spectrum for each of our nine objects to obtain radial velocity, velocity dispersion, mean age and metallicity. We first fit SDSS DR7 spectra of galaxy candidates against a grid of PEGASE.HR (Le Borgne et al. 2004) simple stellar population (SSP) models based on the MILES stellar library (Sánchez-Blázquez et al. 2006) using the NBURSTS pixel space fitting technique (Chilingarian et al. 2007b,a). For every spectrum we first convolve the SSP model grid covering a wide range of ages and metallicities with the instrumental response of the SDSS spectrograph.

Next our minimization procedure convolves the SSP models again with a Gaussian line-of-sight velocity distribution, and multiplies the models by a smooth low-order continuum polynomial aimed at absorbing flux calibration errors in both models and the data. We choose the best-fitting SSP (or a linear combination of two) by interpolating a grid in age and metallicity.

We repeat the fitting procedure to the entire spectrum and to a spectrum with the regions of known emission lines blocked out. We analyze the full available spectral range (from the rest-frame 3640 \AA to 6800 \AA or the red end of the spectrum if it occurs at shorter rest-frame wavelength). If the reduced χ^2 value is significantly lower for the emission-line clipped case, the galaxy has significant emission lines in its spectrum.

In the sample of candidate galaxies, we identify two populations (Table 1). Six galaxies resemble classical elliptical galaxies with ages $t \gtrsim 1 \text{ Gyr}$, high metallicities (from slightly sub-solar to super-solar), and absence of ongoing star formation. Two of these objects are E+As.

Three blue galaxies have young stellar populations ($t < 50 \text{ Myr}$), high-velocity outflows, and sometimes residual star formation (Diamond-Stanic et al. 2012). In one case (SDSSJ112518.89-014532.4, Table 1 and Figure 1) we identify an “extreme post-starburst galaxy”

which we apparently observe immediately after the cessation of a strong and short star formation episode: this object has no prominent emission lines. However, the mean stellar age is $\sim 30 \text{ Myr}$, close to the lowest limit covered by our SSP models. This object is considerably younger than typical E+A galaxies with luminosity weighted ages of 500–800 Myr (Chilingarian et al. 2009; Du et al. 2010).

3.2. HST Imaging Structural Analysis

We process dithered images of the nine galaxies in Table 1 using AstroDrizzle⁴. This image processing step combines individual exposures and rejects spurious pixels (cosmic rays and hot pixels) without changing the native pixel scale. In the special case of SDSSJ123657.44+631115.4, we process the WFC3 IR image to produce a science mosaic with a pixel scale corresponding to the scale of the ACS images.

We characterize the HST surface brightness profiles of our candidates by fitting a set of 2D $R_n^{\frac{1}{n}}$ Sérsic profiles (GALFIT; Peng et al. 2010). Before fitting, we convolve the models with the Tiny Tim PSF (Krist et al. 2011). For many of our candidates there are not enough suitable stars to construct a high signal-to-noise PSF. For targets where a number of stars are available in the image, using the Tiny Tim PSF and the stellar PSF produce very similar results. For consistency, we use the Tiny Tim PSF for all images.

To fit the surface brightness profiles, we start with a single Sérsic profile and simultaneously fit all objects and the sky background in the $\sim 10'' \times 10''$ FoV around our target. With each fitting iteration we enhance the complexity of the model by adding one more Sérsic profile. We repeat fitting until the sky background estimates reach a plateau. Huang et al. (2013) show that this procedure is reliable for large enough regions. If the residual image does not show any prominent structure, we adopt the multiple Sérsic profile as the best fit. With the sky background fixed, we then fit a single Sérsic profile to extract structural parameters for direct comparison with the high- z compact passive systems. The resolution at high redshift limits the fit to a single Sérsic profile. Table 2 lists the parameters of the best-fit multi-component and single-component models.

Figures 1 and 2 show the HST images, the best-fit 2D GALFIT models and residuals, the 1D observed and modeled profiles, and the SDSS spectra and fits for a representative young and old object, respectively. We have applied K plus evolutionary corrections to shift the surface brightness (density) μ profiles to the rest-frame at $z = 0$.

Young Objects: Three systems in this group have composite structure, visible only in the HST images. SDSSJ112518.89-014532.4 is a peculiar young object with only a weak $[\text{O II}]$ line (section 3.1) observed with the HST/WFC3 program targeting recently quenched galaxies with high-velocity gas outflows (Proposal ID 12272: C.Tremonti).

The best-fit model surface brightness profile combines two functions: a compact and an extended Sérsic profile. The largest half-light radius exceeds the one for the

⁴ <http://drizzlepac.stsci.edu>

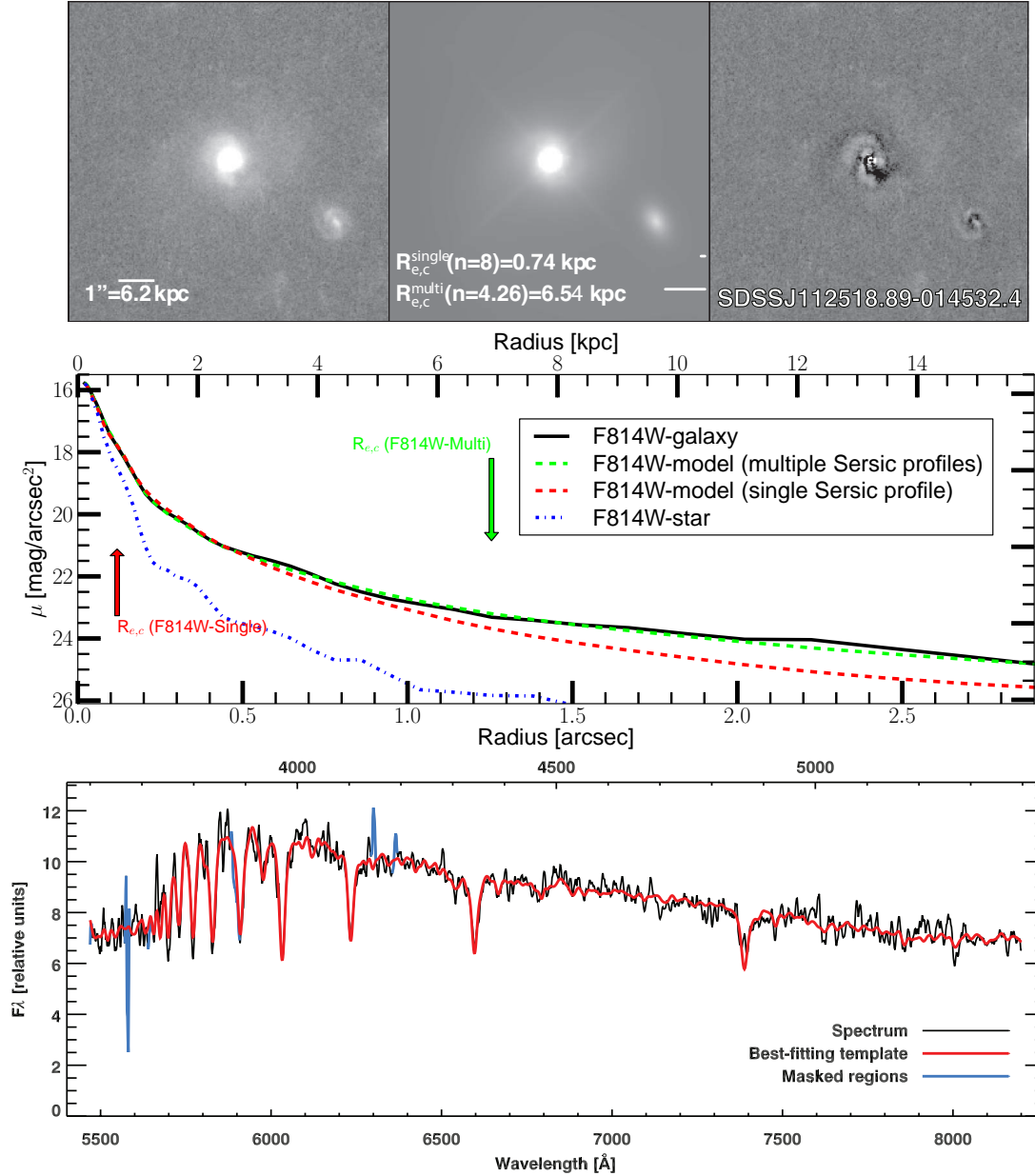


FIG. 1.— A compact intermediate-redshift galaxy dominated by a young stellar population. We show the HST/WFC3 F814W image (top left), the 2D fit (top center), and the residual (top right). The white bars show relevant scales. The central panel shows the 1D observed surface profile (black), the best single (red) and double (green) Sérsic fits, and corresponding half-light radii. We also show the PSF (blue). The bottom panel shows the smoothed SDSS spectrum (black), the best-fit SSP model (red), and the regions excluded from the fit (blue). The bottom axis of this panel shows observed wavelength and the top axis gives galaxy rest-frame wavelength. Note the strong Balmer absorption and absence of prominent emission lines.

best-fit single Sérsic model by a factor of nine ($R_{e,c}^{\text{multi}} = 6.54$ kpc vs. $R_{e,c}^{\text{single}} = 0.74$ kpc, Table 2). The residual map in Fig. 1 shows spiral structure that we do not try to model. Based on the difference between the observed and model surface brightness profiles (Fig 1), at galactocentric distances $R_e \gtrsim 3$ kpc $\approx 4.5 \times R_{e,c}^{\text{single}}$ the multi-profile model describes the observed light profile at low surface brightness levels considerably better than the single Sérsic model. The second component makes no significant difference in the core.

HST images of the other two young systems exhibit similarly complex rest-frame optical morphology. In the most extreme case (SDSSJ150603.69+613148.1) two objects appear in the SDSS images as a single point source. We attribute the SDSS spectrum of this double system, dominated by a young-age SSP, to the larger object containing most of the observed light with the best-fit surface brightness profile parameters in Table 2.

SDSSJ112518.89-014532.4 (Fig. 1) has the highest velocity dispersion in this subsample (σ (SDSSJ112518.89-014532.4) > 200 km s $^{-1}$, Table 1) and its morphology is bulge-dominated. The light profiles for the other two young galaxies are disk-like.

Old Objects : These galaxies generally display much smoother surface brightness profiles. SDSSJ123657.44+631115.4 resides in one of the X-ray luminous clusters targeted by multi-wavelength HST ACS/WFC3 snapshot survey (Proposal ID 12166: H. Ebeling). The abundant HST imaging allows construction of the best-fit 2D models in three filters (F606W, F814W and F110W).

The light profiles in all three bands have very similar Sérsic parameters ($R_{e,c}^{\text{multi}} \approx 3$ kpc, $R_{e,c}^{\text{single}} \approx 1.7$ kpc). We obtain a good fit with only two Sérsic profiles (Table 2). The first row of Figure 2 shows an RGB image composed of two HST ACS images and one rescaled HST WFC3 image. We also plot the corresponding best-fit 2D models and residuals. Radial surface brightness profiles of the models in all three wavelength bands closely follow the observed profile out to $3-4 R_{e,c}$. We note that modeling light profiles for galaxies like this target that are close to the brightest cluster galaxy (BCG) depends critically on the simultaneous modeling of the light profiles for all neighboring systems, including the two-component BCG (e.g., Gonzalez et al. 2005).

The HST morphology of the other five old systems have similar structure. Most of these systems have round shapes and spheroid-like single Sérsic profiles with $n_{\text{Sérsic}}^{\text{single}} > 2.5$.

Like their high- z counterparts (e.g. Bruce et al. 2012; Buitrago et al. 2012), three of these objects have some disk component. One of them, SDSSJ001619.07-003358.8, appears to be an old system with a face-on disk. Based on the best-fit multi-Sérsic model, the surface brightness profile of this system is a combination of two disk profiles. The observed profiles of two other galaxies, SDSSJ123130.98+123224.2 and SDSSJ132950.58+285254.8, display edge-on disk components. The visible light of SDSSJ123130.98+123224.2 is mostly distributed within a disk-like profile (its bulge-to-total ratio is $B/T < 50\%$, based on the best two-component fit). SDSSJ132950.58+285254.8 is a bulge-like object with a weak extended disk ($B/T > 60\%$).

4. STRUCTURAL AND DYNAMICAL PROPERTIES OF COMPACT SYSTEMS AT INTERMEDIATE REDSHIFTS

We combine the parameters of the best-fit single Sérsic model for each galaxy (from Table 2) with measured velocity dispersions (from Table 1) to derive dynamical masses:

$$M_{\text{dyn}} = \frac{\beta(n_{\text{Sérsic}}^{\text{single}})\sigma^2 R_{e,c}^{\text{single}}}{G}, \quad (1)$$

where $\beta(n_{\text{Sérsic}}^{\text{single}})$ is a function of the Sérsic index (Cappellari et al. 2006):

$$\beta(n_{\text{Sérsic}}^{\text{single}}) = 8.87 - 0.831n_{\text{Sérsic}}^{\text{single}} + 0.024(n_{\text{Sérsic}}^{\text{single}})^2. \quad (2)$$

We compare the relations between structural and dynamical properties of our $0.2 < z < 0.6$ sample with the results obtained in two different redshift regimes: $z \lesssim 0.3$ and $0.8 < z < 2.2$. The structural parameters of single-Sérsic models for the low-redshift sample (Table 3; Simard et al. 2011) represent 2D decompositions of the g - and r -band surface brightness profiles for resolved systems in SDSS DR7. Again we require EW[O II] < 5 Å (see section 2). For the $z \sim 0$ sample retrieved from the SDSS DR7 database we also require⁵: i) an average signal-to-noise ratio per pixel of $S/N > 10$ and ii) a measured velocity dispersions in the range $70 \text{ km s}^{-1} < z < 420 \text{ km s}^{-1}$. We include small samples of compact $z \sim 0$ galaxies described in Trujillo et al. (2009) and Taylor et al. (2010). The high-redshift comparison sample is a collection of high-resolution HST imaging and spectroscopic data compiled by van de Sande et al. (2013). All systems in this sample are quiescent galaxies with dynamical masses of $M_{\text{dyn}} > 2 \times 10^{10} M_{\odot}$. We correct measured velocity dispersions for all three samples using the model provided in van de Sande et al. (2013).

The left-hand panel of Figure 3 clearly demonstrates the difference in size between galaxies with similar velocity dispersions at $z \sim 0$ and at $z > 0.2$. For the main $z \sim 0$ comparison sample (gray histogram), the median velocity dispersion is 185 km s^{-1} . For our sample (cyan; $z \sim 0.4$) the median is 178 km s^{-1} and for $z > 1$ (red) the median is 260 km s^{-1} . The corresponding median sizes are 5.9 kpc, 0.74 kpc, and 2.2 kpc, respectively. The median size of $z \sim 0$ sample selected to be compact (gray points) is 1.5 kpc. Although the sizes of our intermediate-redshift compact galaxies are several times smaller than for the $z \sim 0$ systems, velocity dispersions of two samples span the same range of values.

Most of our sample lies in the lower portion of the velocity dispersion range covered by the $z > 1$ sample, but they follow the same trend in size-velocity dispersion parameter space. Furthermore, the intermediate-redshift object with the highest velocity dispersion (Fig. 2) falls very close to the locus of the high-redshift sample.

We note that multiple-profile models tend to overestimate the size of the young morphologically disturbed systems in order to fit their extended asymmetric low-surface-brightness features. Thus the upper limits on the half-light radii derived from the best multi-Sérsic fits

⁵ as recommended at <http://www.sdss.org/dr7/products/spectra/>

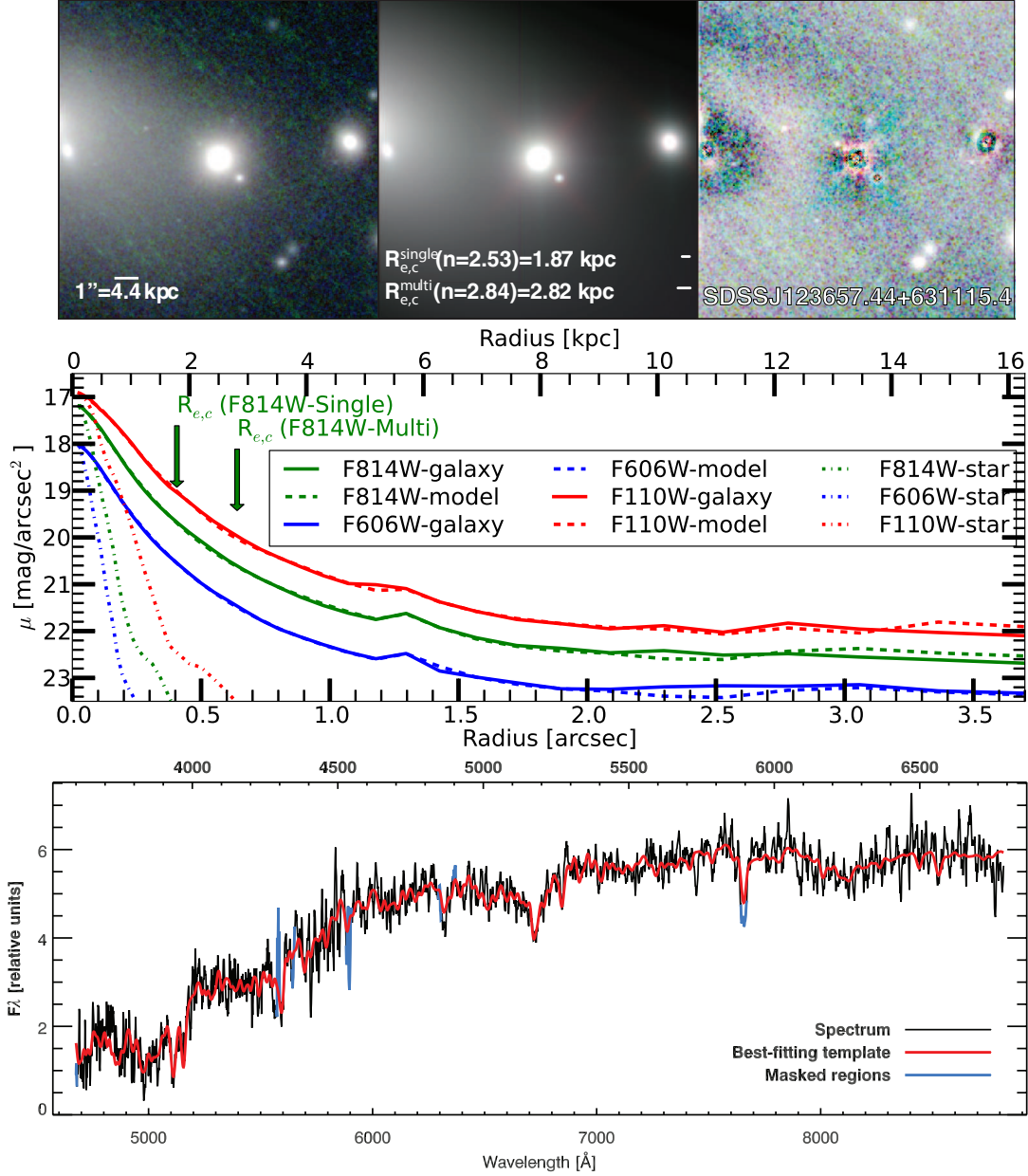


FIG. 2.— A compact massive intermediate-redshift galaxy dominated by an old stellar population. The RGB image (top left) is composed of HST/WFC3 F110W (red), HST/ACS F814W (blue), and HST/ACS F606W (green) light profiles. We also show the RGB image of the best-fit 2D multi-Sérsic profile models in these three filters (middle), and the three-color residual between the observed surface brightness profiles and the models (right). White bars show relevant scales. The central panel shows 1D radial surface brightness profiles (solid lines), the best-fit composite models (dashed lines), and the PSF (dashed-dotted lines). Green arrows denote the half-light radii. The bottom panel shows the smoothed SDSS spectrum (black), the best-fit SSP model (red), and the regions excluded from the fit (blue). The bottom axis of this panel shows observed wavelength and the top axis gives galaxy rest-frame wavelength.

can bring three young compact galaxies in our sample very close to the locus of low-redshift galaxies, but they may be misleading (see the 2D profile in Figure 1).

The right-hand panel of Figure 3 shows a tight size-dynamical mass relation in all three redshift regimes. This relation includes additional information about the Sérsic index of the best-fit profiles (equations 1 and 2). As noted by e.g. van de Sande et al. (2013), there is a clear offset between the loci of $z \sim 0$ and $z > 1$ galaxies in the range of dynamical masses where the two samples overlap ($2 \times 10^{10} M_{\odot} \leq M_{dyn} \leq 1.86 \times 10^{12} M_{\odot}$). In contrast, the sample of compact $z \sim 0$ galaxies overlaps with high-redshift systems. Although our intermediate-redshift galaxies have an average dynamical mass lower than high-redshift quiescent systems ($7.95 \times 10^9 M_{\odot} \leq M_{dyn}(z \sim 0.4) \leq 6.31 \times 10^{11} M_{\odot}$), the two samples follow the same size-dynamical mass relation. The half-light radius of our most extreme target with $\sigma > 300 \text{ km s}^{-1}$ (Fig. 2) is very similar to or even smaller than the average size of similarly massive high-redshift systems. This result suggests that $M_{dyn} \approx 10^{10} M_{\odot}$ compact systems should also exist at $z > 1$, but with half-light radii of $R_{e,c} \approx 0.5 \text{ kpc}$ (or $0''.05$ at $z = 1$) and with currently undetectable extended low surface brightness features.

5. CONCLUSIONS

We identify nine galaxies with dynamical masses of $M_{dyn} \gtrsim 10^{10} M_{\odot}$ as photometric point sources, but with redshifts between $0.2 < z < 0.6$ in the SDSS spectrophotometric database. These nine galaxies have archival HST images demonstrating that they are indeed extremely compact.

It is imperative to track the change in number density of compact systems with redshift, but no meaningful constraint can be derived from our inhomogeneous, serendipitous sample (see Tables 1 and 2). Our sample, however, demonstrates existence: larger samples of intermediate redshift compact quiescent galaxies based on well-defined selection criteria should provide number density estimates.

In size-dynamical-mass parameter space our nine compact galaxies lie away from the typical $z \sim 0$ SDSS galaxies of similar mass. The most massive system in our sample - SDSSJ123657.44+631115.4 - lies right within the locus of massive compact $z > 1$ galaxies. The existence of these serendipitously discovered intermediate redshift compact galaxies provide clues to uncovering larger samples for determining the evolution of dense systems routinely observed at high redshift.

We acknowledge the use of the SDSS DR7 data (<http://www.sdss.org/dr7/>) and the MAST HST database (<http://archive.stsci.edu/hst/>). We thank the referee for prompt, helpful comments. ID is supported by the Harvard College Observatory Menzel Fellowship and NSERC (PDF-421224-2012). The Smithsonian Institution supports the research of IC, HSH, and MJG. IC acknowledges support from grant MD-3288.2012.2.

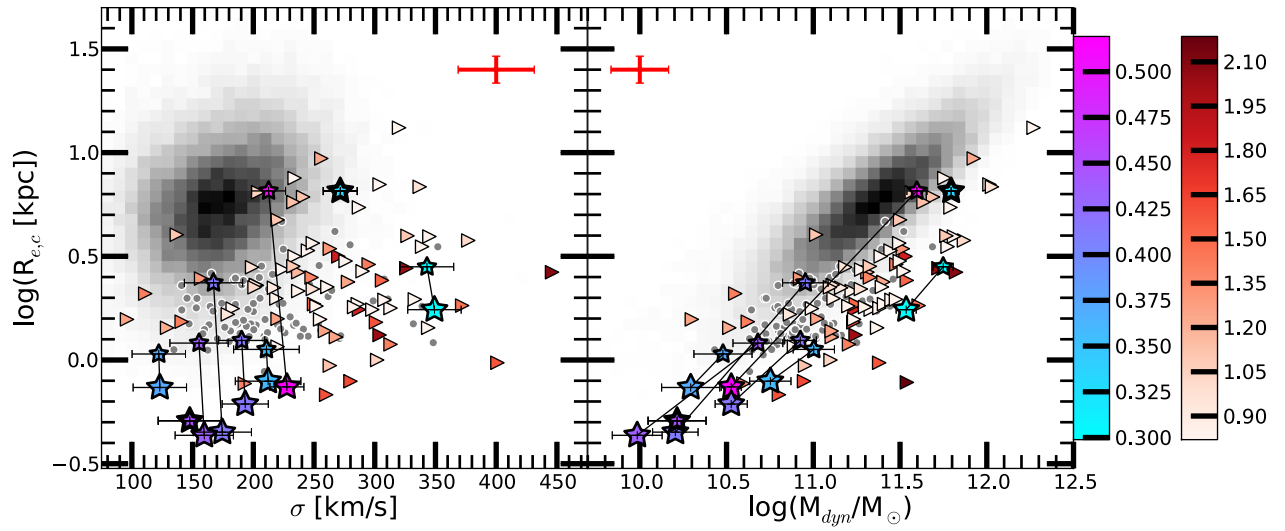


FIG. 3.— The size-velocity dispersion relation (*left*) and the size-dynamical mass relation (*right*) for quiescent galaxies in three redshift ranges: a) $z \lesssim 0.3$ (grey 2D histogram), b) $0.2 < z < 0.6$ (this study, stars), and c) $0.8 < z < 2.2$ (triangles). The symbol color indicates galaxy redshifts according to the color bars. Two points connected by a solid line represent each target in our sample: the smaller circularized half-light radii $R_{e,c}$ (larger star) corresponds to the single-Sérsic profile and the larger $R_{e,c}$ (smaller star) denotes the upper limit from the largest $R_{e,c}$ in the multi-Sérsic profile. The red bar shows the average error for the high-redshift sample. The grey points denote the $z \sim 0$ compact sample (Trujillo et al. 2009; Taylor et al. 2010).

REFERENCES

- Ahn, C. P. and Alexandroff, R. and Allende Prieto, C. and Anders, F. and Anderson, S. F. and Anderton, T. and Andrews, B. H. and Aubourg, É. and Bailey, S. and Bastien, F. A. et al. 2013, ArXiv e-prints, arXiv:1307.7735
- Bezanson, R., van Dokkum, P. G., Tal, T., Marchesini, D., Kriek, M., Franx, M., & Coppi, P. 2009, *The Astrophysical Journal*, 697, 1290
- Bruce, V. A., et al. 2012, *Monthly Notices of the Royal Astronomical Society*, 427, 1666
- Buitrago, F., Trujillo, I., Conselice, C. J., Bouwens, R. J., Dickinson, M., & Yan, H. 2008, *The Astrophysical Journal*, 687, L61
- Buitrago, F., Trujillo, I., Conselice, C. J., & Haussler, B. 2012, *Monthly Notices of the Royal Astronomical Society*, 428, 1460
- Cappellari, M., et al. 2006, *Monthly Notices of the Royal Astronomical Society*, 366, 1126
- Carollo, C. M., et al. 2013, *The Astrophysical Journal*, 773, 112
- Carrasco, E. R., Conselice, C. J., & Trujillo, I. 2010, *Monthly Notices of the Royal Astronomical Society*, 405, 2253
- Cassata, P., et al. 2011, *The Astrophysical Journal*, 743, 96
- Chilingarian, I., Prugniel, P., Sil'chenko, O., & Koleva, M. 2007a, in *IAU Symposium, Vol. 241, Stellar Populations as Building Blocks of Galaxies*, ed. A. Vazdekis & R. R. Peletier (Cambridge, UK: Cambridge University Press), 175–176, arXiv:0709.3047
- Chilingarian, I. V., De Rijcke, S., & Buyle, P. 2009, *ApJ*, 697, L111
- Chilingarian, I. V., Sil'chenko, O. K., Afanasiev, V. L., & Prugniel, P. 2007b, *Astronomy Letters*, 33, 292
- Cimatti, A., et al. 2008, *Astronomy and Astrophysics*, 482, 21
- Daddi, E., et al. 2005, *The Astrophysical Journal*, 626, 680
- Damjanov, I., et al. 2009, *The Astrophysical Journal*, 695, 101
- . 2011, *The Astrophysical Journal Letters*, 739, L44
- Diamond-Stanic, A. M., Moustakas, J., Tremonti, C. A., Coil, A. L., Hickox, R. C., Robaina, A. R., Rudnick, G. H., & Sell, P. H. 2012, *The Astrophysical Journal*, 755, L26
- Du, W., Luo, A., Prugniel, P., Liang, Y.-C., & Zhao, Y.-H. 2010, *Monthly Notices of the Royal Astronomical Society*, 409, 567
- Fan, L., Lapi, A., De Zotti, G., & Danese, L. 2008, *The Astrophysical Journal Letters*, 689, L101
- Gonzalez, A. H., Zabludoff, A. I., & Zaritsky, D. 2005, *The Astrophysical Journal*, 618, 195
- Hopkins, P. F., Bundy, K., Hernquist, L., Wuyts, S., & Cox, T. J. 2010, *Monthly Notices of the Royal Astronomical Society*, 401, 1099
- Huang, S., Ho, L. C., Peng, C. Y., Li, Z.-Y., & Barth, A. J. 2013, *The Astrophysical Journal*, 766, 47
- Khochfar, S., & Silk, J. 2006, *The Astrophysical Journal*, 648, L21
- Krist, J. E., Hook, R. N., & Stoehr, F. 2011, in *Optical Modeling and Performance Predictions V*. Edited by Kahan Mark A. *Proceedings of the SPIE*, ed. M. A. Kahan, Vol. 8127, 81270J–81270J–16
- Le Borgne, D., Rocca-Volmerange, B., Prugniel, P., Lançon, A., Fioc, M., & Soubiran, C. 2004, *A&A*, 425, 881
- Mancini, C., et al. 2010, *Monthly Notices of the Royal Astronomical Society*, 401, 933
- Naab, T., Johansson, P. H., & Ostriker, J. P. 2009, *The Astrophysical Journal*, 699, L178
- Newman, A. B., Ellis, R. S., Bundy, K., & Treu, T. 2012, *The Astrophysical Journal*, 746, 162
- Nipoti, C., Treu, T., Auger, M., & Bolton, A. 2009, *The Astrophysical Journal Letters*, 706, L86
- Onodera, M., et al. 2012, *The Astrophysical Journal*, 755, 26
- Oser, L., Ostriker, J. P., Naab, T., Johansson, P. H., & Burkert, A. 2010, *The Astrophysical Journal*, 725, 2312
- Peng, C. Y., Ho, L. C., Impey, C. D., & Rix, H.-W. 2010, *The Astronomical Journal*, 139, 2097
- Poggianti, B. M., et al. 2013, *The Astrophysical Journal*, 762, 77
- Ragone-Figueroa, C., & Granato, G. L. 2011, *Monthly Notices of the Royal Astronomical Society*, 414, 3690
- Saglia, R. P., et al. 2010, *Astronomy and Astrophysics*, 524, A6
- Sánchez-Blázquez, P., et al. 2006, *MNRAS*, 371, 703
- Saracco, P., Longhetti, M., & Gargiulo, A. 2011, *Monthly Notices of the Royal Astronomical Society*, 412, 2707
- Shankar, F., Marulli, F., Bernardi, M., Mei, S., Meert, A., & Vikram, V. 2012, *Monthly Notices of the Royal Astronomical Society*, 428, 109
- Simard, L., Trevor Mendel, J., Patton, D. R., Ellison, S. L., & McConnell, A. W. 2011, *The Astrophysical Journal Supplement Series*, 196, 11
- Strazzullo, V., et al. 2010, *Astronomy & Astrophysics*, 524, A17
- Szomoru, D., Franx, M., & van Dokkum, P. G. 2012, *The Astrophysical Journal*, 749, 121
- Taylor, E. N., Franx, M., Glazebrook, K., Brinchmann, J., van der Wel, A., & van Dokkum, P. G. 2010, *The Astrophysical Journal*, 720, 723
- Toft, S., et al. 2007, *The Astrophysical Journal*, 671, 285
- Trujillo, I., Cenarro, a. J., de Lorenzo-Cáceres, A., Vazdekis, A., de la Rosa, I. G., & Cava, A. 2009, *The Astrophysical Journal*, 692, L118
- Trujillo, I., Conselice, C. J., Bundy, K., Cooper, M. C., Eisenhardt, P., & Ellis, R. S. 2007, *Monthly Notices of the Royal Astronomical Society*, 382, 109
- Valentinuzzi, T., et al. 2010a, *The Astrophysical Journal*, 721, L19
- . 2010b, *The Astrophysical Journal*, 712, 226
- van de Sande, J., et al. 2013, *The Astrophysical Journal*, 771, 85
- van Dokkum, P. G., et al. 2008, *The Astrophysical Journal*, 677, L5
- Zirm, A. W., et al. 2007, *The Astrophysical Journal*, 656, 66

TABLE 1
 SPECTROSCOPIC PROPERTIES

ID	z	σ_{obs} [km s ⁻¹]	$\frac{\sigma_{obs}}{\sigma}$	Age [Myr]	[Z/H] [dex]	SDSS Program/Target	Comment
(1)	(2)	(3)	(4)	(5)	(6)	(7)	(8)
SDSSJ001619.07-003358.8	0.37199	114 ± 22	0.9268/0.9333	538 ± 18	0.56 ± 0.15	Southern/ QSO_HIZ	Old (E+A)
SDSSJ100218.66+143757.0	0.33049	272 ± 14	1.0015/1.0015	> 8900	-0.05 ± 0.07	Legacy/ GALAXY_RED	Old
SDSSJ112518.89-014532.4	0.51926	210 ± 14	0.9225/0.9880	35 ± 2	-0.53 ± 0.11	Legacy/ QSO_SKIRT	Young
SDSSJ123130.98+123224.2	0.41553	178 ± 19	0.9207/0.9348	1448 ± 122	-0.33 ± 0.19	Legacy/ QSO_HIZ	Old
SDSSJ123657.44+631115.4	0.29884	331 ± 22	0.9480/0.9650	> 8900	-0.01 ± 0.08	Legacy/ GALAXY_RED, ROSAT_D	Old
SDSSJ132950.58+285254.8	0.35661	197 ± 27	0.9285/0.9346	1229 ± 161	0.22 ± 0.20	Legacy/ QSO_HIZ	Old
SDSSJ135920.98+513738.9	0.41292	159 ± 24	0.9115/0.9509	20 ± 1	0.14 ± 0.13	Legacy/ QSO_CAP, SERENDIP_BLUE	Young
SDSSJ143026.34+342944.6	0.44704	135 ± 26	0.9142/0.9142	954 ± 85	-0.06 ± 0.23	Legacy/ QSO_HIZ	Old (E+A)
SDSSJ150603.69+613148.1	0.43680	145 ± 24	0.9086/0.9336	32 ± 1	-0.20 ± 0.15	Legacy/ QSO_SKIRT	Young

NOTE. — Columns: (1) SDSS designation; (2) Redshift; (3) Observed velocity dispersion; (4) Aperture correction for single-/multi-Sérsic profile (see Table 2); (5) Age of the best-fit SSP model; (6) Metallicity of the best-fit SSP model; (7) SDSS target flag; (8) Classification

 TABLE 2
 STRUCTURAL PROPERTIES

ID	$R_{e,c}^{single}$ [kpc]	$n_{Sérsic}^{single}$	$(b/a)^{single}$	$R_{e,c}^{multi}$ [kpc]	$n_{Sérsic}^{multi}$	$(b/a)^{multi}$	N	HST program/camera/filter (pixel scale ["/pix])	Comment
(1)	(2)	(3)	(4)	(5)	(6)	(7)	(8)	(9)	(10)
SDSSJ0016-0033	0.74	1.63	0.78	1.07	0.91	0.92	2	10555/ACS/F625W (0.05)	disk
SDSSJ1002+1437	6.53	4.58	0.85	6.53	4.58	0.85	1	10084/WFPC2/F606W (0.10)	bulge
SDSSJ1125-0145	0.74	8.00	0.90	6.54	4.26	0.70	2	12272/WFC3 /F814W (0.04)	bulge-dominated
SDSSJ1231+1232	0.61	3.42	0.16	1.24	1.04	0.14	2	5370/WFPC2/F814W (0.10)	disk-dominated
SDSSJ1236+6311 or	1.76	2.53	0.94	3.25	2.76	0.95	2	12166/ACS/F606W (0.05)	bulge-dominated
SDSSJ1236+6311 or	1.75	2.53	0.94	2.81	2.03	0.98	2	12166/ACS/F814W (0.05)	bulge-dominated
SDSSJ1236+6311	1.65	2.20	0.94	2.55	2.78	0.98	2	12166/WFC3/F110W (0.128)	bulge-dominated
SDSSJ1329+2852	0.79	2.65	0.38	1.13	0.25	0.16	3	10626/ACS/F814W (0.05)	bulge-dominated
SDSSJ1359+5137	0.45	5.47	0.86	2.36	4.09	0.89	4	12019/WFC3/F814W (0.04)	disk-dominated ^a
SDSSJ1430+3429	0.51	3.36	0.53	0.51	3.36	0.53	2	10890/WFPC2/F606W (0.1)	bulge-dominated ^b
SDSSJ1506+6131	0.43	8.00	0.75	1.21	2.30	0.64	2	12019/WFC3/F814W (0.04)	disk-dominated

 NOTE. — Columns: (1) SDSS designation (abridged); (2) Circularized half-light radius of the single-profile model ($R_{e,c}^{single} = R_e^{single} \times \sqrt{b/a}$, where R_e is the major axis half-light radius and b/a is the axial ratio); (3) Sérsic index of the single-profile model; (4) Axial ratio of the single-profile model; (5) The largest (circularized) half-light radius of the composite model; (6) Sérsic index corresponding to (5); (7) Axial ratio corresponding to (5); (8) Number of profiles in the composite model; (9) HST program ID, camera and filter (corresponding pixel scale); (10) Morphology.

^a The largest component in this multi-Sérsic fit has a de Vaucouleurs profile, but the inner three disk-like components with $n \approx 2$ dominate the observed light profile.

^b This object requires two Sérsic profiles fitted simultaneously: a disk and a more prominent bulge with similar half-light radii.